Research Article

Cr_2O_3/rGO nanocomposite with excellent electrochemical capacitive properties

Imran Shafi[1] · Yuanyue Liu[2] · Gaojie Zeng[1] · Zijiong Li[2] · Baojun Li[3] · Erjun Liang[1]

Received: 23 June 2020 / Accepted: 7 October 2020 / Published online: 17 October 2020
© Springer Nature Switzerland AG 2020

Abstract
Herein, we have reported the excellent electrochemical capacitive properties of the Cr_2O_3/rGO nanocomposite synthesized by hydrothermal. After the structural authentication by Raman spectroscopy and XRD studies, the Cr_2O_3/rGO nanocomposite was probed under different physicochemical techniques. It is found that due to good structural congruity between Cr_2O_3 nanoplates and rGO, the electrochemical properties of Cr_2O_3/rGO nanocomposite have strong synergistic effects. As a result, an unprecedented pseudocapacitance of Cr_2O_3/rGO nanocomposite is revealed at extremely small scan rate (0.1–1.1 mV s^{-1}). At higher scan rate (10–50 mV s^{-1}), the charge/discharge behavior (in CV) of the Cr_2O_3/rGO nanocomposite is found to be oriented towards the ordinary known properties of the commercial Cr_2O_3 however, the charge storage capacity is still very high. Furthermore, very high theoretical charge storage capacity (93% at 50 mV s^{-1}), high specific capacitance (556 F g^{-1}/310 F g^{-1} at 0.75 A g^{-1}/1.75 A g^{-1} (GCD) and 635 F g^{-1} at 1.1 mV s^{-1} (CV) respectively) and excellent cyclic retention (92% of the initial value after 3500 cycles) was obtained for the Cr_2O_3/rGO nanocomposite. The EIS test (Nyquist plot) is in good agreement with the aforementioned results.

Keywords Pseudocapacitance · Cr_2O_3/rGO nanocomposite · Charge storage capacity · CV · GCD

1 Introduction

In order to deal with contemporary challenges of increasing demand for electrical energy storage (EES), the development of more efficient, reliable and environmental friendly devices have become need of the hour. Among the available EES devices, batteries and capacitors are of utmost importance. Although, a high energy density is featured by the batteries but they have a couple of drawbacks: a low power density and slow charge rate. On the other hand, capacitors meet many desired properties including faster charge/discharge capability, higher specific capacitance, higher specific power density and excellent cyclic life [1, 2]. In this context, the supercapacitors have received significant attention in last decade and many different materials have been investigated for supercapacitor application. Generally, on the basis of their working principle and the internal structure, supercapacitors are classified into two major types, electric double-layer capacitors (EDLCs) and pseudocapacitors or faradic capacitors [3]. In EDLCs, energy is stored on the surface of the electrode without chemical reaction taking place while in pseudocapacitors the energy is stored by both the surface controlled processes and reversible faradic reactions [4,

Electronic supplementary material The online version of this article (https://doi.org/10.1007/s42452-020-03636-8) contains supplementary material, which is available to authorized users.

✉ Erjun Liang, ejliang@zzu.edu.cn; Zijiong Li, zijiongl@126.com | [1]Key Laboratory of Materials Physics of Ministry of Education of China, School of Physics and Microelectronics, Zhengzhou University, Zhengzhou 450001, China. [2]School of Physics and Electronic Engineering, Zhengzhou University of Light Industry, Zhengzhou 450001, China. [3]College of Chemistry, Zhengzhou University, Zhengzhou 450001, China.

5]. Pseudocapacitors are found to have the higher energy densities mainly due to the redox reactions taking place at the surface of electrode materials such as conducting polymers [6–8] and transition metal oxides (TMOs) such as NiO, RuO_2, Fe_2O_3, MnO_2, etc.[9–14]. Like many other materials, the TMOs display more redox reactions due to their multiple oxidation states [15].

Therefore, being widely available, environmental friendly and electrochemically compatible, the Cr_2O_3 is widely investigated for its potential application in lithium ion batteries [16, 17]. Except batteries, it has been widely applied in other fields, such as catalysts, gas sensors and magnetic applications [18–20]. Similarly, due to some of its promising properties (given in above lines), it is also applied for supercapacitor application. To date, only a few reports on the use of Cr_2O_3 for supercapacitor application are available in literature in which the Cr_2O_3 nanocomposites were reported to have both, the surface controlled and diffusion limited redox reactions [21–24]. However, the capacitance values reported are far below the required level which hereby indicates that it is a challenging task to obtain high electrochemical capacitive outcomes from the Cr_2O_3. The main obstacle in this regard is its poor electrical conductivity and small BET area. On the other hand, graphene is known due to its promising electrical conductivity and high Brunauer–Emmett–Teller (BET) area and appears as an ideal companion for the nanoscale TMOs including Cr_2O_3 to improve its electrochemical performance [25–28].

In this context, we have synthesized the Cr_2O_3/rGO nanocomposite by a hydrothermal route and conducted its electrochemical screening. At extremely small scan rate, the current response is found proportional to the potential throughout the charging/discharging cycle in the CV, which resulted in an unprecedented pseudocapacitance of Cr_2O_3/rGO nanocomposite with a large CV surface area. Similarly, by increasing the scan rate, the electrode has shown excellent polarization behavior with increasing current response and an extended potential window, however, the charge/discharge tendency is found to move toward the ordinary Cr_2O_3 behavior in which sharp faradaic peaks are associated with small surface area. Ideal supercapacitor behavior is displayed by the Cr_2O_3/rGO nanocomposite in GCD results for smaller current densities and very high specific capacitance from both the CV and GCD curves is computed.

2 Experimental

2.1 Synthesis of materials

All the reagents used in this work were purchased from Shanghai Macklin Biochemical Co., Ltd. China and used directly without further purification.

2.2 Synthesis of the rGO

GO was prepared by modified Hummer's method from natural graphite in a two-step process. Briefly, graphite powder (1.5 g) was first immerged into concentrated sulfuric acid [H_2SO_4 (50.7 mL)] placed in an ice bath along with sodium nitrate [$NaNO_3$ (1.14 g)]. Potassium permanganate [$KMnO_4$ (6 g)] was then added slowly with stirring for 2 (h). After 72 h, 150 mL solution of H_2SO_4 (5%) was added and then the reactants were terminated to an addition of 30% H_2O_2. At this stage, the color of the solution was changed into bright yellow. The mixture was ultrasonicated for 20 min and then washed with hydrochloric acid [HCL (10%)] in order to remove the metal ions. Finally, the mixture was washed several times with water led by ethanol absolute and a solid product was obtained in a cold environment at low temperature. The as prepared GO was then reduced by chemical method (through hydrazine treatment) to get rGO [29]. Briefly, GO powder was mixed in purified water (1 mg / ml) in a flask. Immediately after mixing, hydrazine monohydrate (1 µ l / 3 mg of GO) was inducted into the mixture and the mixture was placed at 80° C in oil bath under stirring for 12 h. After which, the resulting product was obtained through centrifugation at a frequency of 10,000 RPM.

2.3 Synthesis of the Cr_2O_3/rGO nanocomposite

The rGO suspension was prepared in double deionized water (DDW) followed by ultrasonication for 1 h. Similarly, Na_2CrO_4 was mixed in DDW and ultrasonicated for 1 h. Later on, rGO and Na_2CrO_4 were mixed to form a secondary solution (75 mL). The required ratio was prepared by keeping rGO and Na_2CrO_4 (1: 3). After which the secondary solution was stirred for 30 min and then the pH of the solution was adjusted to 2 by adding the droplets of HCl. The suspension was aged for several hours at 60° C in water bath. After which the same suspension was transferred into a Teflon-lined stainless steel autoclave (100 mL) and was kept at 150 °C for 24 h. The resulting product was washed with deionized water and absolute ethanol for several times. The final product was collected by centrifugation (10,000 RPM) and dried at room temperature in vacuum oven for 24 h. The dried Cr_2O_3/rGO

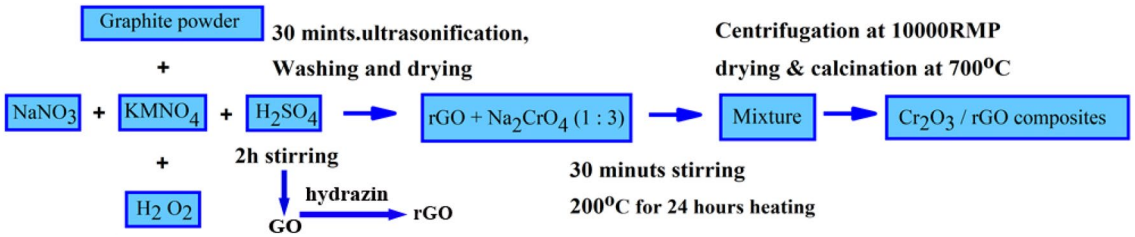

Scheme 1 The schematic illustration for the synthesis of the Cr_2O_3/rGO nanocomposite.

composite were then calcinated at 500 °C for 4 h in Ar environment. The schematic illustration for the synthesis of the Cr_2O_3/rGO nanocomposites is shown in Scheme. 1.

2.4 Fabrication of the working electrodes

The pretreated Ni-foam strip was pressed under a suitable pressure for 10–15 s and then the active mass (Cr_2O_3/rGO composites) was loaded on it by droplet method in which two drops of the active slurry were loaded gently on 1 cm^2 of the electrode and dried in vacuum oven at 60 °C for 8 h. The loadable material was consists of an active mass, carbon black and polytetrafluoroethylene (PTFE) with the ratio 90: 5: 5. The loaded electrodes were dried over night to become fully dry. Later, the dry electrodes were soaked in 2 M KOH aqueous solution for 10 h and then examined for the electrochemical performance.

2.5 Characterizations

The structural and compositional analyses were carried out by using the Raman spectroscopy and the X–ray diffraction (XRD). Raman spectrum was acquired by using a LabRAM HR Evolution Raman spectrometer (HORIBA Jobin Yvon S.A.A.) with 532 nm laser wavelength excitation and XRD was performed between 10°—80° at a voltage (V) = 40 kV and current (I) = 30 mA with a Ni—filtered Cu—Kα radiation. The energy band gap of the Cr_2O_3/rGO nanocomposite was analyzed by ultraviolet–visible (UV—vis) spectrophotometer. The surface morphology of the samples was observed by a scanning electron microscopy (SEM) while the size and the shape of the materials were analyzed by a tunneling electron microscopy (TEM) JEOL JEM (2100 F) under an accelerating potential of 200 kV. The BET surface area and the pore size of the rGO and the Cr_2O_3/rGO nanocomposite were evaluated by N_2—adsorption/desorption isotherms. Zahner-Ennium—E_4 (German) work station was used for electrochemical measurements (CV, GCD and EIS) in 2 M KOH solution without any prepurging.

3 Results and discussion

3.1 Material characterization

The Raman spectrum for the Cr_2O_3/rGO nanocomposite is shown in Fig. 1a. The peak P_4 located around 550 cm^{-1} is attributed to the stretching vibrations of Cr–O (A_{1g}) [30] while the peaks P_1—P_3 and P_5 located at 296 cm^{-1}, 350 cm^{-1}, 528 cm^{-1} and 615 cm^{-1} are identified as E_{1g} modes. All these peaks are termed as Raman active modes for Cr_2O_3 [31, 32]. The two peaks observed at 1370 cm^{-1} and 1590 cm^{-1} are referred to *D* and *G* bands (sp^3 and sp^2 hybridized C—C modes). The existence of the *D* and *G* bands in Cr_2O_3/rGO nanocomposite, which is consistent with the isolated rGO spectrum in Fig. 1a and confirms the presence of reduced graphene oxide in the nanocomposites. Generally, the intensity ratio of the *D* and *G* bands (I_D/I_G) is used to determine the quality of carbon nanomaterials [33]. Its lower value indicates a higher crystallinity of the structures or vice versa. For the Cr_2O_3/rGO nanocomposite, it has been reported 1.8 [34] whereas, it is 1.04 in present study, suggesting a better crystallinity of the nanocomposites.

The XRD patterns of rGO and Cr_2O_3/rGO nanocomposite are shown in the Fig. 1b. The XRD pattern of Cr_2O_3/rGO nanocomposite reveals the rhombohedral symmetry of nano Cr_2O_3 (space group R-3c, a = 0.4957 nm, b = 0.4957 nm and c = 1.3592 nm, JCPDS card no. 81 – 0314). It is noteworthy that the appearance of an extra peak, corresponding to the (002) plane of the stacked graphene sheet at 2θ = 26° [35], witnesses the presence of the graphene in Cr_2O_3/rGO composite [34]. Moreover, greater intensity of the (104) than that of the (110) plane suggests the material being oriented towards the (104) plane. More active sites are provided for this orientation during the insertion/deinsertion process of OH^{-1} [3]. The UV—vis absorption spectra of rGO, commercial Cr_2O_3 and Cr_2O_3/rGO nanocomposite are shown Fig. 1c and their energy band gaps are obtained accordingly (Fig. 1d).

It can be seen that the energy band gap of the commercial Cr_2O_3 is 3.04 eV however, for the Cr_2O_3/rGO nanocomposite synthesized in present study, it is 2.47 eV. This smaller value may be due to the induction of rGO (with

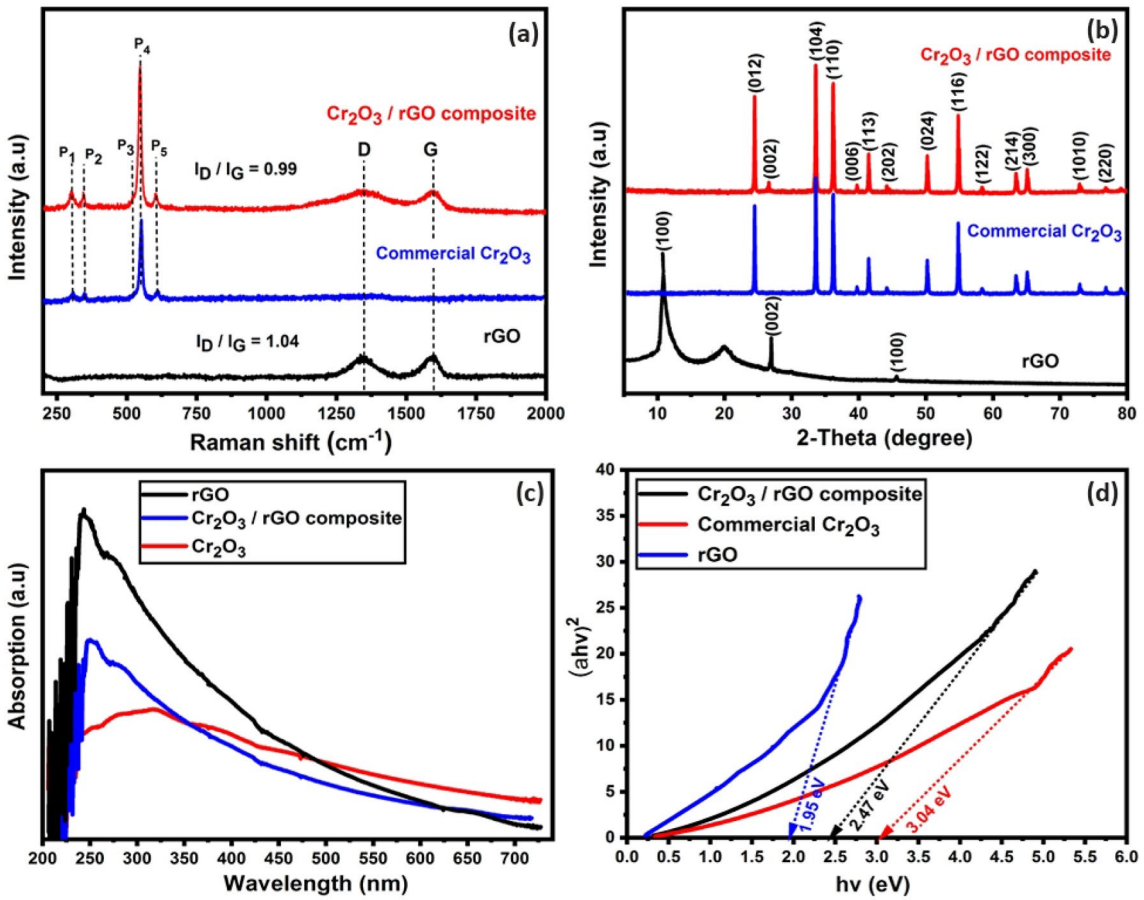

Fig.1 **a** The Raman spectra of rGO and Cr_2O_3/rGO nanocomposite, **b** The XRD patterns of rGO and Cr_2O_3/rGO nanocomposite, **c** The UV–vis absorption data of the rGO, commercial Cr_2O_3 and Cr_2O_{30}/rGO nanocomposite and **d** The energy band gap of the rGO, Cr_2O_3 and Cr_2O_3/rGO nanocomposite

energy band gap of 1.95 eV) into Cr_2O_3 nanoplates, which is in agreement with the results of [36] and indicates the semiconductor nature of the Cr_2O_3/rGO nanocomposite. By the analogy of these results with [37, 38], it may be concluded that the rGO has good contact and possibly forms heterojunctions with Cr_2O_3 nanoplates. The introduction of rGO in conducting metals is one of the strategies to enhance the electronic conductivity of the composites through formation of heterojunctions which leads to a reduced bang gap and high conductivity of the composite [39]. A suitable energy band gap facilitates the transfer of the electrons between conduction and valence bands during the faradaic reactions and improves charge storage and hence the capacitance.

The surface morphology, shape and size of the materials are given in SEM and TEM images shown in Fig. 2a-f. Figure 2a is the surface morphology of as prepared GO while, Fig. 2(b) shows the surface morphology of rGO. Similarly, the surface morphology of Cr_2O_3/rGO nanocomposite is shown in Fig. 2(c), which verifies the presence of rGO and Cr_2O_3 on the surface. Figure 2(d) is the TEM image of rGO while, Fig. 2(e and f) are the TEM images of Cr_2O_3/rGO nanocomposite at 200 nm and 50 nm respectively. The well ordered structures of the Cr_2O_3/rGO nanocomposite is depicted by both, Fig. 2(e and f). Further, the EDS image given in Fig. 2(g) shows that the At % of carbon and oxygen are 68.40 and 31.60 respectively.

The BET area is a very important parameter regarding electrochemical energy storage. A high BET area leads towards a high performance. The BET area of 25, 170 and 265 $m^2\ g^{-1}$ for commercial Cr_2O_3, rGO, and Cr_2O_3/rGO nanocomposite are shown in Fig. 3a, c and e while, the corresponding pore size distribution is given in Fig. 3b, d and f. The Fig. 3e shows a type—IV of the isotherm [40] which suggests the existence of a range of pore size, i.e. The adsorption / desorption hysteresis from the relative pressure of 0.1–0.8 indicates the existence of the mesopores on the surface of the Cr_2O_3/rGO nanocomposite while, the presence of the micropores is witnessed by a vertical tail near the relative pressure "1".

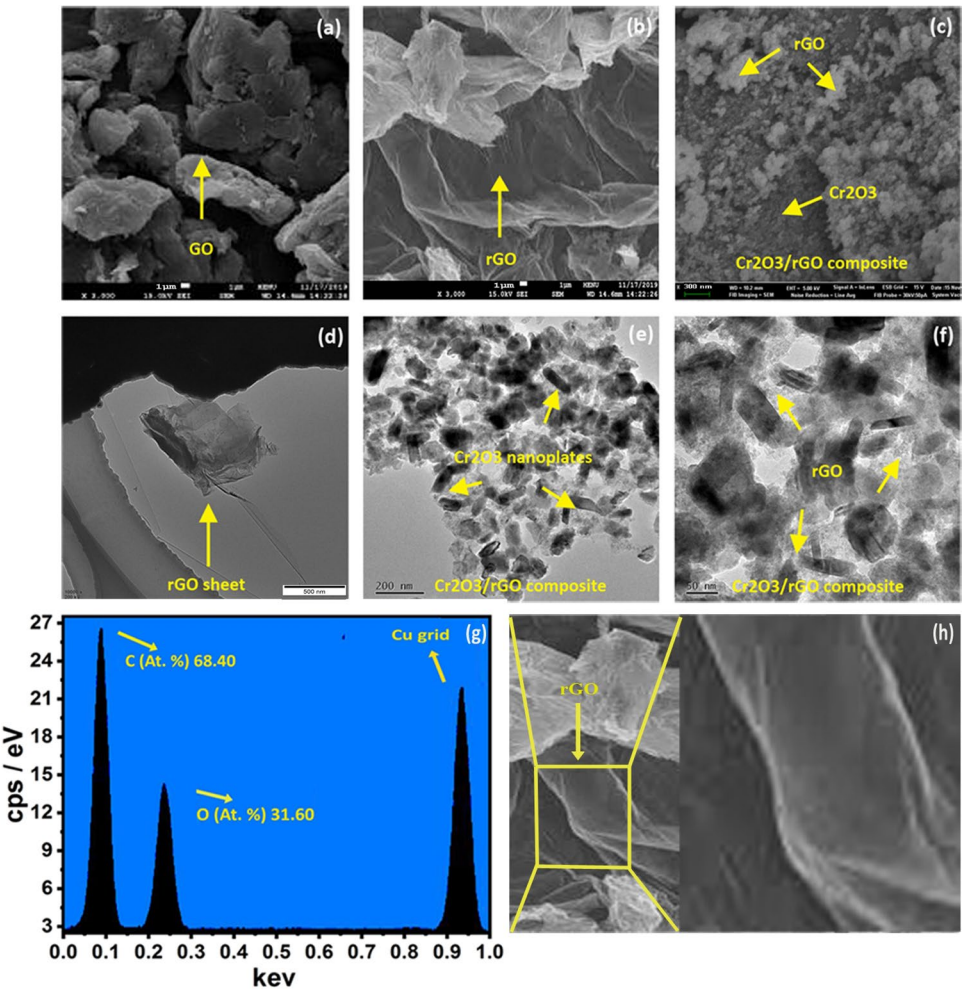

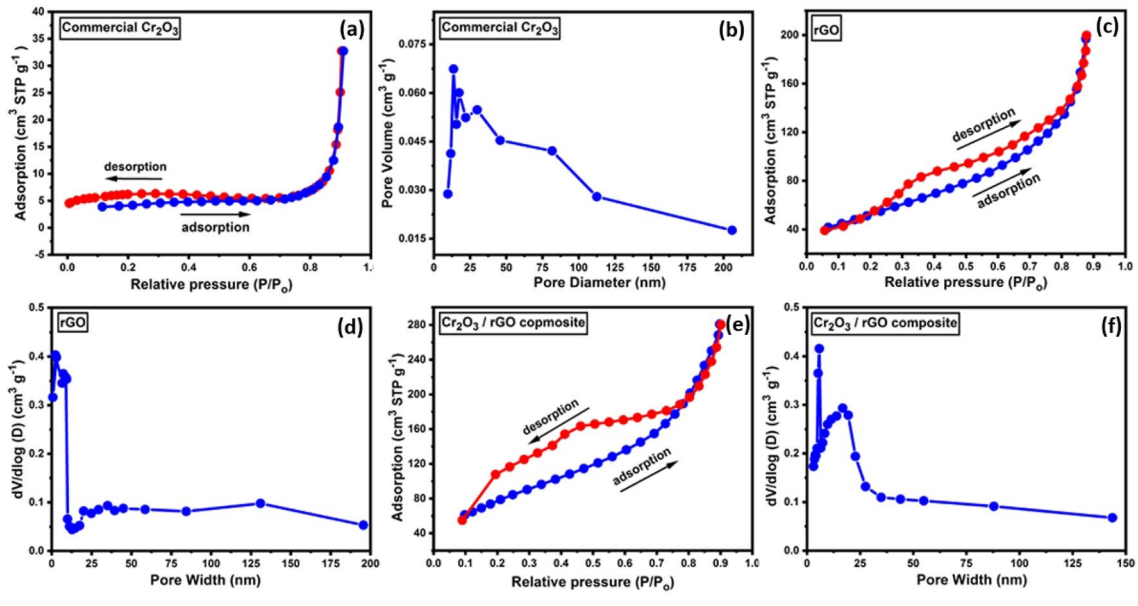

Fig.2 **a–c** The SEM images of as prepared GO, rGO and Cr_2O_3/rGO nanocomposite, **d** The TEM image of rGO at 500 nm and **e–f** The TEM images of Cr_2O_3/rGO nanocomposite at 200 nm and 50 nm, respectively, **g** The EDS image of rGO for the focused area shown in **h**

Fig.3 **a, c** and **e** The adsorption / desorption curves for commercial Cr_2O_3, rGO and Cr_2O_3/rGO nanocomposite respectively and **b, d** and **f** The pore size distribution for Cr_2O_3, rGO and Cr_2O_3/rGO nanocomposite respectively

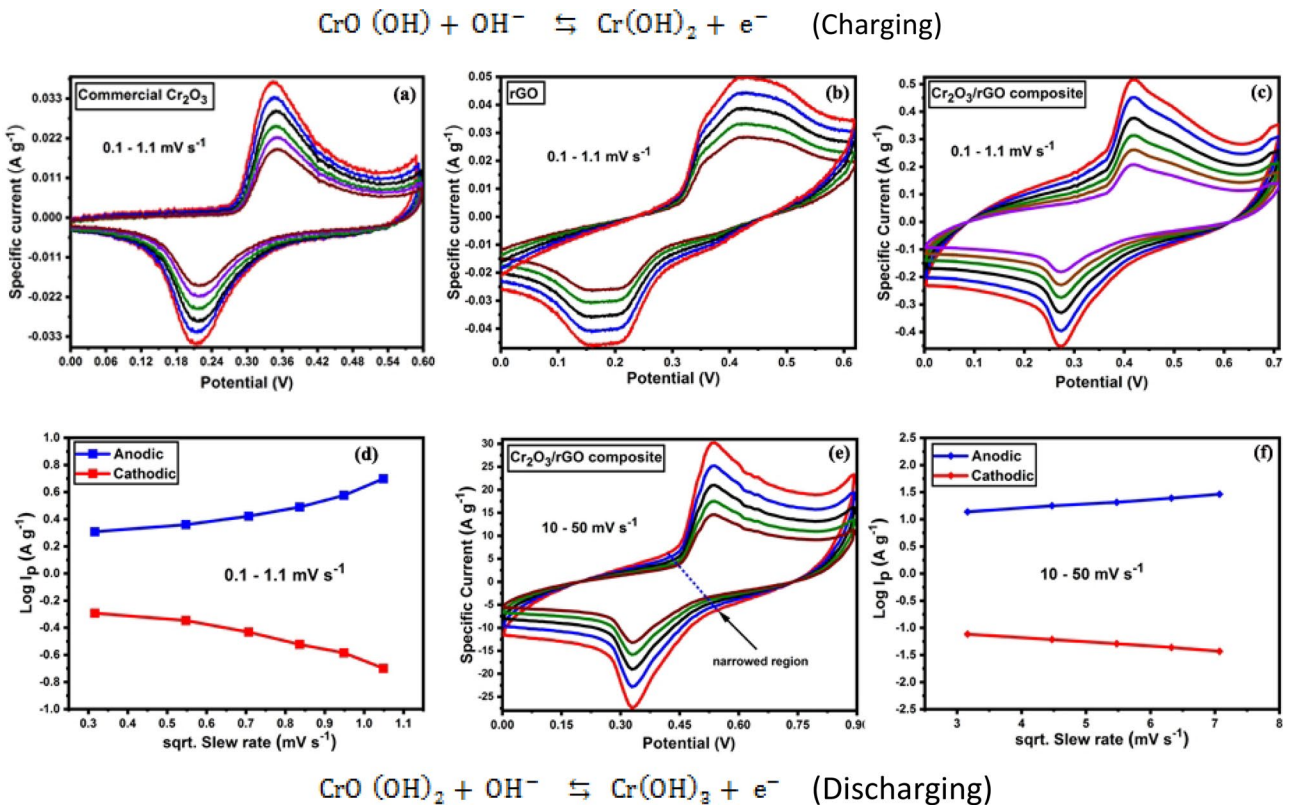

Fig. 4 **a–c** The CV pattern of commercial Cr_2O_3, rGO and Cr_2O_3/rGO nanocomposite at 0.1—1.1 mV s^{-1} respectively, **d** The log. (I_{peak}) vs. log. scan rate for Cr_2O_3/rGO nanocomposite at 0.1 – 1.1 mV s^{-1}, **e** The CV pattern for Cr_2O_3/rGO nanocomposite from 10—50 mV s^{-1} and **f** The log. (I_{peak}) vs. log. scan rate for Cr_2O_3/rGO nanocomposite at 10 – 50 mV s^{-1}

3.2 Electrochemical Screening

The CV curves of the commercial Cr_2O_3, rGO and Cr_2O_3/rGO nanocomposite performed at extremely small scan range from 0.1 to 1.1 mV s^{-1} are shown in Fig. 4a, b, c respectively. Figure 4a shows that there is no current response up to 0.26 V (of 0.50 V) and then there are well known abrupt oxidation/reduction reactions for commercial Cr_2O_3. As a result, the commercial Cr_2O_3 has conventional narrow redox peaks which make it a suitable faradaic material, but its surface area (hence surface capacitance) is very small with limited potential window. Similarly, the current response of rGO in Fig. 4b is linear with potential up to 0.30 V (of 0.62 V) and then there is a multi—state charge/discharge process. Though the peaks of rGO in Fig. 4b are not as sharp as commercial Cr_2O_3, but the potential window is significantly extended along with a higher current response and the faradaic peaks are broadened which give rise to an enhanced CV surface area (hence the surface capacitance too). It is important to mention here that the electrochemical study of the isolated rGO electrode (both in CV and GCD) in present work is just to visualize its intermediary role physically. The Fig. 4c shows the charge / discharge tendency of Cr_2O_3/rGO nanocomposite at the same scan range, which is quite different as compared with commercial Cr_2O_3 in Fig. 4a. The current in Fig. 4c is directly proportional to the scan potential throughout the charge / discharge cycle for Cr_2O_3/rGO nanocomposite. There are well maintained broader redox peaks with a large CV surface area in Fig. 4c, which indicates that the total current (hence the surface capacitance too) is increased significantly. From the general observation of Fig. 4a, b, c, it is clear that rGO has produced a strong synergistic effect [41] with the electrochemical features of Cr_2O_3 nanoplates to develop a rectangular CV for Cr_2O_3/rGO nanocomposite. The logarithm of peak current (A g^{-1}) verses square root of the scan rate (mV s^{-1}) for Cr_2O_3/rGO nanocomposite from 0.1 to 1.1 mV s^{-1}, which manifests a rapid increase in current is shown in Fig. 4d.

Additionally, the CV curves for the Cr_2O_3/rGO nanocomposite from 10—50 mV s^{-1} are also recorded and shown in Fig. 4e. The proportionality of current with potential is not sustained now. There is a significant decrease in current from 0 to 0.45 V in Fig. 4e and as a result, the CV is being narrowed at central part, while the faradaic peaks become sharp. However, the potential window and peak current is

still increasing with the scan rate which emphasize good reversibility of the reactions at electrode's surface [42–44]. The logarithm of peak current (A g^{-1}) verses square root of the scan rate (mV s^{-1}) for Cr_2O_3/rGO nanocomposite from 10—50 mV s^{-1} is shown in Fig. 4f, in which the log. (I_{peak}) is linearly proportional to the logarithmic scan rate, suggesting the reaction being surface limited [45, 46], however, the rate of increase in the charge storage is decreasing for higher scan rates.

The surface capacitance of the Cr_2O_3/rGO nanocomposite at a rate of 1.1 mV s^{-1} (m = 0.6 mg) is computed 635 F g^{-1} which is reduced to 551 F g^{-1} at a scan rate of 50 mV s^{-1}. Along with the excellent electrode performance at such a high scan rate, the surface capacitance results also explicate the consequence of increase in the scan rate as decline in surface capacitance with a shift in charge/discharge behavior. The surface capacitance can be calculated by the following equation,

$$C = \frac{S_2 - S_1}{2mk(U_1 - U_2)} = \frac{S}{2mk(U_1 - U_2)} \quad (1)$$

where k is the scan rate, S_1 and S_2 are the discharging/charging integrated area relative to the horizontal axis, U_1 and U_2 are the initial and final potentials respectively, S is the net surface area and m the active mass. The surface reactions during the charging/discharging can be attributed to the conversions from Cr^{3+} to Cr^{4+} and vice versa, according to the following chemical equations [47, 48],

$$CrO(OH) + OH^- \leftrightarrows Cr(OH)_2 + e^- \text{ (Charging)}$$

$$CrO(OH)_2 + OH^- \leftrightarrows Cr(OH)_3 + e^- \text{ (Discharging)}$$

Being semiconducting nature, the CV behavior of Cr_2O_3/rGO nanocomposite may be better explained according to the electrochemistry of semiconductors. The mutual change in the current and corresponding potential can be expressed by Nernst and Randles–Sevcik equation,

$$I = \frac{n^2F^2A\Gamma_t v\, e\left[\frac{(E-E^O)nF}{RT}\right]}{RT\left(1 + e\left[\frac{(E-E^O)nF)}{RT}\right]\right)} \quad (2)$$

where n is the number of electrons transfer between the oxidized and reduced sites, F is the Faraday's constant, A is the electrode's area, v is the scan potential rate, T is the temperature, R is the gas constant and $\Gamma_t = \Gamma_0 + \Gamma_r$ the total area covered by the oxidized and reduced sites. For the CV of Cr_2O_3/rGO nanocomposite shown in Fig. 4c, the peak potential difference for oxidation and reduction states is very small (0.14 V), which illustrates that the redox centers may be interactive (electron's donation and acceptance takes place at close potentials) with each other due to their good electronic conductivity and very short gap between them. The electrons for a suitable potential jumps into conduction band from the valence band and results delocalized electron pseudocapacitance [49]. Moreover, the aforementioned results also provide hints that there are both; diffusion and capacitive controlled reactions on the surface of electrode during charging / discharging process [50]. In this context, we have analyzed the total current response and the results are presented in Fig. 5a, b.

The b value governed by the power law of current $i = av^b$ for Cr_2O_3/rGO nanocomposite at a scan range from 10 to 50 mV s^{-1} is 0.9 which authenticate the capacitive nature of the total charge storage in this range while, Fig. 5b shows that the Cr_2O_3/rGO nanocomposite has delivered a capacitive current of 93% at a scan rate of 50 mV s^{-1} according to the equation for total curren $i(v) = k_1 v^{\frac{1}{2}} + k_2 v$

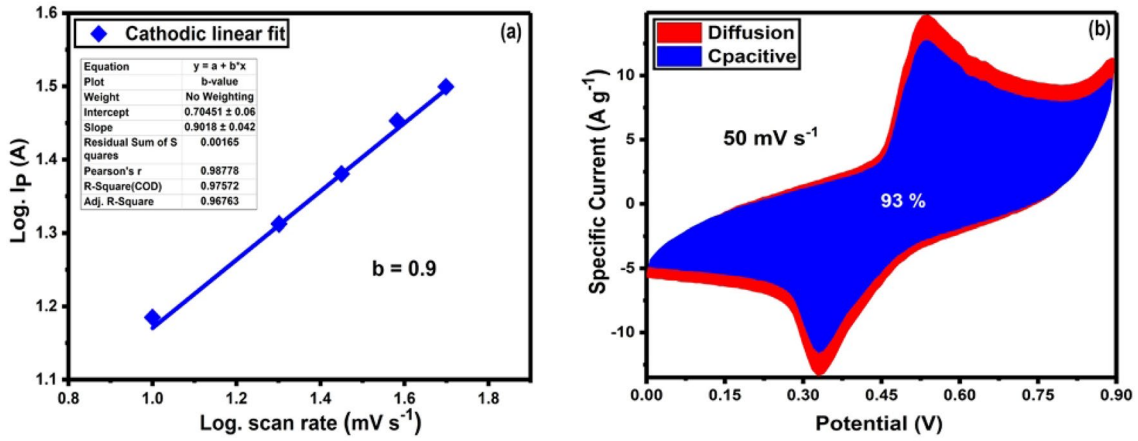

Fig. 5 **a** Logarithm plot of the peak specific current verses logarithmic scan rate for 10 – 50 mV s^{-1} and **b** The capacitive and diffusion controlled current at 50 mV s^{-1}

[50]. The results shown in Fig. 5a, b emphasize that the Cr_2O_3/rGO nanocomposite may be a suitable candidate for supercapacitor application. The comparison of the present work with similar previous reports on Cr_2O_3 and Cr_2O_3 nanocomposites is given in [S_2].

The GCD curves of commercial Cr_2O_3, rGO and Cr_2O_3/rGO nanocomposite at current density from 0.75 to 1.75 A g^{-1} are given in Fig. 6a, b, c, respectively. The charging / discharging process for commercial Cr_2O_3 in Fig. 6a is the result of abrupt reactions (similar to Fig. 4a) while, a multi-state (similar to Fig. 4b) charging/discharging cycle with better capacity is observed for rGO is shown in Fig. 6b. The GCD curves of commercial Cr_2O_3 have obvious discharge losses, indicating that the reactions at the surface of the electrode are not fully reversible and the actual discharge energy is only a portion of total charging energy whereas, the GCD curves of rGO given an intermediary view. Nevertheless, the energy loss region disappears in GCD profiles of Cr_2O_3/rGO nanocomposite and the fairly balanced energy charge/discharge results, which are desired for supercapacitor electrodes [51], are obtained in Fig. 6c. In Fig. 6d, an ideal supercapacitor behavior is highlighted in a triangular section in which the charging energy E_1 is balanced by the discharging energy E_2 for Cr_2O_3/rGO nanocomposite. The emergence of the associated regions R-I and R-II aside reveals pseudocapacitance [52] during charging/discharging processes, which is responsible for the balanced energy and high performance.

The cycling lifetime is a challenging issue in the capacitive systems. It is demonstrated that the Cr_2O_3/rGO nanocomposite gives rise to an excellent cycling retention of 92% after 3500 charge/discharge cycles, which is much higher than the commercial Cr_2O_3 (65%) electrode as shown in Fig. 6e. The Nyquist plot for Cr_2O_3/rGO nanocomposite is given in Fig. 6f. The equivalent series resistance (ESR) obtained from the intercept of the semi-circle is 0.55 ohms, which is increased to 0.81 ohms after 3500 cycles. Further, the ending tail is very close to vertical (90°) which indicates the excellent capacitive nature of the Cr_2O_3/rGO composite [53]. The results are in accordance with the Maxwell—Wagner model [54], according to which, the small increase in ESR witnesses the existence of purely conducting grain boundaries in the material. A comparison of the present work with the similar results in literature is given in Table 1.

The higher electrochemical performance may be associated with faster ionic transport with the mesoporous nature of the Cr_2O_3/rGO nanocomposite which can play ensuing role in achieving the high electrochemically active BET area. Moreover, the higher pore volume of 0.826 cm^3 g^{-1} for the Cr_2O_3/rGO nanocomposite may also favorable for faster ionic diffusion thereby providing more electrochemically active sites during the charging/discharging

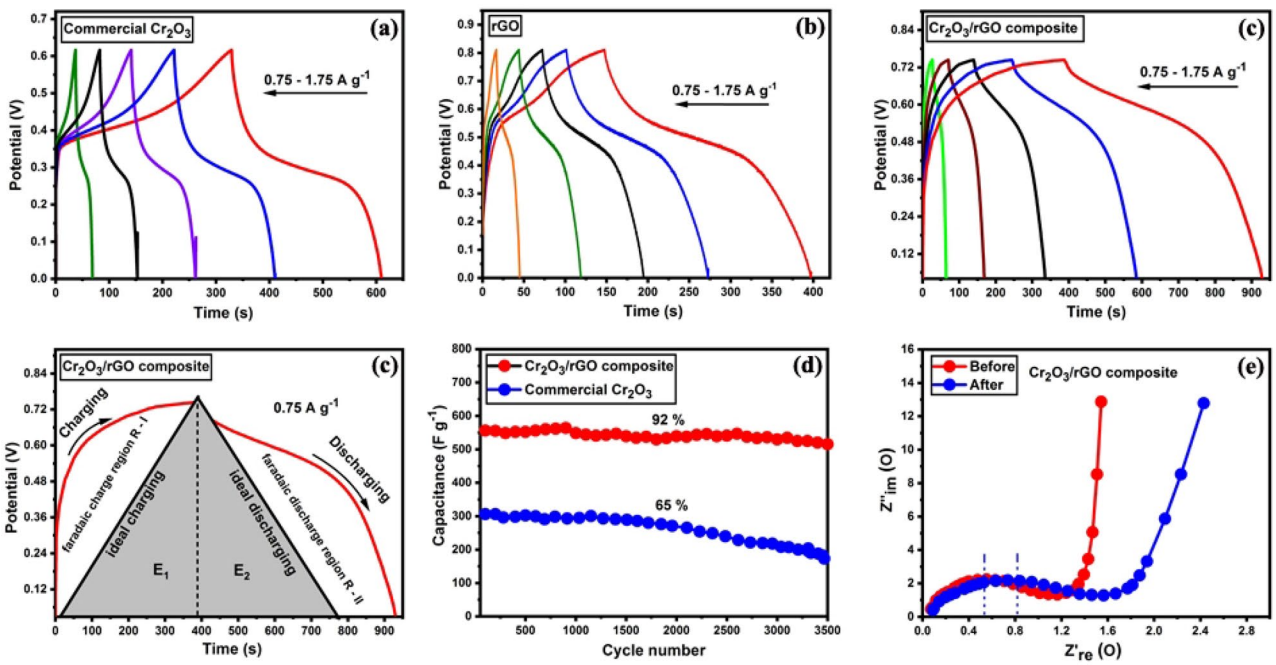

Fig. 6 **a–c** The GCD results for commercial Cr_2O_3, rGO and Cr_2O_3/rGO nanocomposites at a current density from 0.75—1.75 A g^{-1}, respectively, **d** Explication of the charge / discharge process of Cr_2O_3/rGO nanocomposites at 0.75 A g^{-1}, **e** The cycling retention of commercial Cr_2O_3, rGO and Cr_2O_3/rGO nanocomposites after 3500 cycles and **f** Nyquist plots for Cr_2O_3/rGO nanocomposites before and after 3500 cycles

Table 1 The comparison of the present work with the other Cr_2O_3 and Cr_2O_3-composites used as electrode materials for supercapacitors

Materials	Synthesis methods	Specific Capacitance (F g^{-1} (GCD))	Specific current (A g^{-1})	Electrolyte (KOH, M)	Reference
Cr_2O_3 nanoparticles	Hydrothermal	340	0.5	1	[24]
Cr_2O_3/	Carbonization	291	0.25	6	[22]
C Cr_2O_3/MWCNTs	Hydrothermal	257	0.25	1	[3]
Cr_2O_3/rGO	Hydrothermal	556/310	0.75/1.75	2	Present work

process. Therefore, the porous nature, high pore volume and high BET area are most likely responsible for enhancing the electrochemical performance of the Cr_2O_3/rGO nanocomposite [41]

4 Conclusions

The Cr_2O_3/rGO nanocomposite with promising electrochemical characteristics were synthesized by a hydrothermal method successfully. By the induction of rGO into Cr_2O_3 nanoplates, the unprecedented pseudocapacitance of Cr_2O_3/rGO nanocomposite was revealed at extremely small scan range, which was turned towards the ordinary Cr_2O_3 behavior with decreasing surface capacitance for higher scan rates. Very high percentage of capacitive current is separated from the noncapacitive effects in a CV profile. The fairly balanced GCD curves for Cr_2O_3/rGO nanocomposite were observed. Exceptionally high values of the surface and GCD based specific capacitance along with an excellent cycling retention after 3500 cycles were obtained for Cr_2O_3/rGO nanocomposite. This work including the preparation method and nanostructure will lead towards the development of the pseudosupercapacitors in future.

Acknowledgements This work was supported by National Natural Science Foundation of China (Nos.11574276, 11874328).

Compliance with ethical standards

Conflict of interest The authors declare that they have no conflict of interest.

References

1. Oakes L, Westover A, Mares JW, Chatter Jee S, Erwin WR, Bardhan R, Weiss SM, Pint CL (2013) Surface engineered porous silicon for stable, high performance electrochemical supercapacitors. Sci. Rep 3:3020
2. Conway BE, Super-capacitors E (1999) Scientific fundamentals and technological applications. Electrochemical Super-capacitors. Springer, Boston, pp 417–477
3. Chen B, Wang Y, Li C, Fu L, Liu X, Zhu Y, Zhang L, Wu Y (2017) A Cr_2O_3/MWCNTs composite as a superior electrode material for supercapacitor. RSC Adv 7(40):25019–25024
4. Bose S, Kuila T, Mishra AK, Rajasekar R, Kim NH, Lee JH (2012) Carbon-based nano-structured materials and their composites as supercapacitor electrodes. J Mater Chem A 22(3):767–784
5. Simon P, Gogotsi Y (2010) Materials for electrochemical capacitors In nanoscience and technology. Nat Rev Mater. https://doi.org/10.1142/9789814287005_0033
6. Wang JG, Kang F, Wei B (2015) Engineering of MnO_2-based nanocomposites for high performance supercapacitors. Prog Mater Sci 74:51–124
7. Khosrozadeh A, Darabi MA, Xing M, Wang Q (2016) Flexible electrode design: fabrication of freestanding polyaniline-based composite films for high-performance super-capacitors. ACS Appl Mater Interfaces 8(18):11379–11389
8. Liu S, Wang F, Dong R, Zhang T, Zhang J, Zheng Z, Mai Y, Feng X (2017) Soft-template construction of 3D macroporous polypyrrole scaffolds. Small 13(14):1604099
9. Al-Enizi AM, Ubaidullah M, Ahmed J, Ahamad T, Ahmad T, Shaikh SF, Naushad M (2020) Synthesis of NiOx@ NPC composite for high-performance supercapacitor via waste PET plastic-derived Ni-MOF. Compos B Eng 183:107655
10. Hu Y, Zhang Y, Yuan D, Li X, Cai Y, Wang J (2017) Controllable structure transitions of Mn_3O_4 nano-materials and their effects on electrochemical properties. Nanoscale Horiz 2(6):326–332
11. Yu F, Zhu L, You T, Wang F, Wen Z (2015) Preparation of chestnut-like porous NiO nanospheres as electrodes for super-capacitors. RSC Advances 5(116):96165–96169
12. Jin H, Qian J, Zhou L, Yuan J, Huang H, Wang Y, Tang WM, Chan HLW (2016) Suppressing the coffee-ring effect in semitransparent MnO_2 film for a high-performance solar-powered energy storage window. ACS Appl Mater Interfaces 8(14):9088–9096
13. Liu Y, Zhang B, Yang Y, Chang Z, Wen Z, Wu Y (2013) Polypyrrole-coated α-MoO_3 nano-belts with good electrochemical performance as anode materials for aqueous supercapacitors. J Mater Chem A 1(43):13582–13587
14. Guo Y, Li J, Chen M, Gao G (2015) Facile synthesis of vanadium pentoxide carbon core-shell nano-wires for high-performance supercapacitors. J Power Sourc 273:804–809
15. Cuan J, Zhou Y, Zhang J, Zhou T, Liang G, Li S, Yu X, Pang WK, Guo Z (2019) Multiple anionic transition-metal oxycarbide for better lithium storage and facilitated multielectron reactions. ACS Nano 13(10):11665–11675
16. Liu H, Du X, Xing X, Wang G, Qiao SZ (2012) Highly ordered mesoporous Cr_2O_3 materials with enhanced performance for gas sensors and lithium ion batteries. Chem Commun 48(6):865–867
17. Zhang XZ, Han D, He YB, Zhai DY, Liu D, Du H, Li B, Kang F (2016) Mesoporous Cr_2O_3 nanotubes as an efficient catalyst for Li–O_2 batteries with low charge potential and enhanced cyclic performance. J Mat Chem A 4(20):7727–7735

18. Kohli N, Singh O, Singh RC (2012) Sensing behaviour of tin doped chromium oxide gas sensor toward ethanol. Appl Phys A 109(3):585–590
19. Lei S, Peng X, Liang Z, Li X, Wang C, Cheng B, Xiao Y, Zhou L (2012) Self-template formation and properties study of Cr_2O_3 nano tubes. J Mater Chem 22(4):1643–1651
20. Wang Z, Alrehaily L, Joseph J, Wren JC, Wang J, Sham TK (2017) Scanning transmission X-ray microscopy studies of chromium hydroxide hollow spheres and nanoparticles formed by gamma radiation. Can J Chem 95(11):1146–1150
21. Kharade PM, Thombare JV, Kadam SL, Kulkarni SB, Salunkhe DJ (2017) Layered PPy/Cr_2O_3 as a supercapacitor electrode with improved electrochemical performance. J Mater Sci 28(23):17908–17916
22. Ullah S, Khan IA, Choucair M, Badshah A, Khan I, Nadeem MA (2015) A novel Cr_2O_3 carbon composite as a high performance pseudo-capacitor electrode material. Electrochim Acta 171:142–149
23. Zhu J, Jiang Y, Lu Z, Zhao C, Xie L, Chen L, Duan J (2017a) Single-crystal Cr_2O_3 nanoplates with differing crystalinities, derived from tri-nuclear complexes and embedded in a carbon matrix, as an electrode material for supercapacitors. J colloid interface sci 498:351–363
24. Shafi I, Liang E, Li B (2020) Ultrafine chromium oxide (Cr_2O_3) nanoparticles as a pseudocapacitive electrode material for supercapacitors. J Alloys Comp 851:156046
25. Askari MB, Salarizadeh P, Seifi M, Rozati SM, Beheshti-Marnani A (2020) Binary mixed molybdenum cobalt sulfide nanosheets decorated on rGO as a high-performance supercapacitor electrode. Nanotechnology 31(27):275406
26. Salarizadeh P, Askari MB, Seifi M, Rozati SM, Eisazadeh SS (2020) Pristine $NiCo_2O_4$ nanorods loaded rGO electrode as a remarkable electrode material for asymmetric supercapacitors. Mater Sci Semicond Process 114:105078
27. Wang H, Yang Y, Liang Y, Robinson JT, Li Y, Jackson A, Cui Y, Dai H (2011) Graphene-wrapped sulfur particles as a rechargeable lithium-sulfur battery cathode material with high capacity and cycling stability. Nano Lett 11(7):2644–2647
28. Liang Y, Li Y, Wang H, Zhou J, Wang J, Regier T, Dai H (2011) Co_3O_4 nano - crystals on graphene as a synergistic catalyst for oxygen reduction reaction. Nat Mater 10(10):780
29. Park S, An J, Potts JR, Velamakanni A, Murali S, Ruoff RS (2011) Hydrazine-reduction of graphite-and graphene oxide. Carbon 49(9):3019–3023
30. Khamlich S, Manikandan E, Ngom BD, Sithole J, Nemraoui O, Zorkani I, McCrindle R, Cingo N, Maaza M (2011) Synthesis, characterization, and growth mechanism of α-Cr_2O_3 mono-dispersed particles. J. Phys. Chem. Solids 72(6):714–718
31. Zuo J, Xu C, Hou B, Wang C, Xie Y, Qian Y (1996) Raman Spectra of Nanophase Cr_2O_3. J Raman spectrosc 27(12):921–923
32. Xu H, Zeng M, Li J (2015a) Graphene-wrapped Cr_2O_3 hollow nanospheres with enhanced electrochemical performances for lithium-ion batteries. Int J Electrochem Sci 10:7361–7370
33. Dresselhaus MS, Jorio A, Souza Filho AG, Saito R (2010) Defect characterization in graphene and carbon nanotubes using Raman spectroscopy. Philos Trans Royal Soc A 368(1932):5355–5377
34. Xu H, Zeng M, Li J (2015b) Graphene-wrapped Cr_2O_3 hollow nano-spheres with enhanced electrochemical performances for lithium-ion batteries. Int J Electrochem Sci 10:7361–7370
35. Zhou G, Wang DW, Li F, Zhang L, Li N, Wu ZS, Wen L, Lu GQ, Cheng HM (2010) Graphene-wrapped Fe_3O_4 anode material with improved reversible capacity and cyclic stability for lithium ion batteries. Chem Mater 22(18):5306–5313
36. Ekwealor ABC (2014) Variations of optical and structural properties with temperature for cr_xo_y thin films synthesized in a polymer matrix by chemical bath deposition technique. DIG J of NANOMATER and BIOS 9(1):423–431
37. Jana A, Scheer E, Polarz S (2017) Synthesis of graphene-transition metal oxide hybrid nanoparticles and their application in various fields. Beilstein J Nanotechnol 8(1):688–714
38. Wu C, Shen Q, Mi R, Deng S, Shu Y, Wang H, Liu J, Yan H (2014) Three-dimensional Co_3O_4/flocculent graphene hybrid on Ni foam for supercapacitor applications. J Mater Chem A 2(38):15987–15994
39. Li X, Shen R, Ma S, Chen X, Xie J (2018) Graphene-based heterojunction photocatalysts. Appl Surf Sci 430:53–107
40. Cao Z, Qin M, Jia B, Zhang L, Wan Q, Wang M, Volinsky AA, Qu X (2014) Facile route for synthesis of mesoporous Cr_2O_3 sheet as anode materials for Li-ion batteries. Electrochim Acta 139:76–81
41. Saraf M, Rajak R, Mobin SM (2016) A fascinating multitasking Cu-MOF/rGO hybrid for high performance supercapacitors and highly sensitive and selective electrochemical nitrite sensors. J Mat Chem A 4(42):16432–16445
42. Jiang Y, Chen L, Zhang H, Zhang Q, Chen W, Zhu J, Song D (2016) Two-dimensional Co_3O_4 thin sheets assembled by 3D interconnected nano-flake array framework structures with enhanced supercapacitor performance derived from coordination complexes. Chem. Eng. Sci 292:1–12
43. Conway BE, Birss V, Wojtowicz J (1997) The role and utilization of pseudocapacitance for energy storage by supercapacitors. J Power Sourc 66(1–2):1–14
44. Gupta V, Miura N (2005) Electrochemically deposited polyaniline nano-wire's network a high-performance electrode material for redox super-capacitor. Electrochem Solid State Lett 8(12):A630–A632
45. Simon P, Gogotsi Y, Dunn B (2014) Where do batteries end and supercapacitors begin? Science 343(6176):1210–1211
46. Augustyn V, Come J, Lowe MA, Kim JW, Taberna PL, Tolbert SH, Abruña HD, Simon P, Dunn B (2013) High-rate electrochemical energy storage through Li^+ intercalation pseudocapacitance. Nat Mater 12(6):518
47. Zhu J, Jiang Y, Lu Z, Zhao C, Xie L, Chen L, Duan J (2017b) Single-crystal Cr_2O_3 nano-plates with differing crystalinities, derived from tri-nuclear complexes and embedded in a carbon matrix, as an electrode material for super-capacitors. J Colloid Interface Sci 498:351–363
48. Cummings CY, Attard GA, Mitchels JM, Marken F (2012) Surface state trapping and mobility revealed by junction electrochemistry of nano-cr_2o_3. Aust J Chem 65(1):65–71
49. Chen GZ (2013) Understanding supercapacitors based on nanohybrid materials with interfacial conjugation. Prog Nat Sci Mat Int 23:245–255
50. Brezesinski T, Wang J, Tolbert SH, Dunn B (2010) Ordered mesoporous α-MoO_3 with iso-oriented nano-crystalline walls for thin-film pseudocapacitors. Nat Mater 9(2):146
51. Guan L, Yu L, Chen GZ (2016) Capacitive and non-capacitive faradaic charge storage. Electrochim Acta 206:464–478
52. Peng C, Jin J, Chen GZ (2007) A comparative study on electrochemical co-deposition and capacitance of composite films of conducting polymers and carbon nanotubes. Electrochim Acta 53:525–537
53. Yan J, Wei T, Shao B, Ma F, Fan Z, Zhang M, Zheng C, Shang Y, Qian W, Wei F (2010) Electrochemical properties of graphene nanosheet/carbon black composites as electrodes for supercapacitors. Carbon 48(6):1731–1737
54. Wagner KW (1913) Dissipation of energy under AC. Ann. Phys 40:817–855

Publisher's Note Springer Nature remains neutral with regard to jurisdictional claims in published maps and institutional affiliations.